Soil Dynamics and Earthquake Engineering 190 (2025) 109235

Contents lists available at ScienceDirect

Soil Dynamics and Earthquake Engineering

journal homepage: www.elsevier.com/locate/soildyn

Modeling near-surface velocity inversion in a sediment sequence using microtremor HVSR

Dhananjay A. Sant [a,*], Gunjankumar K. Makwana [a], Prabhin Sukumaran [b], Imtiyaz A. Parvez [c,**], Govindan Rangarajan [d], K. Krishnan [e]

[a] Department of Geology, Faculty of Science, The Maharaja Sayajirao University of Baroda, Vadodara, 390002, India
[b] Dr. K.C. Patel Research and Development Centre, Charotar University of Science and Technology (CHARUSAT), Changa, Anand, Gujarat, 388421, India
[c] CSIR Fourth Paradigm Institute, NAL Belur Campus, Bengaluru, 560 037, India
[d] Department of Mathematics, Indian Institute of Science, Bangalore, 560 012, India
[e] Department of Archaeology and Ancient History, Faculty of Arts, The Maharaja Sayajirao University of Baroda, Vadodara, 390 002, India

ARTICLE INFO

Keywords:
Ambient noise
Microtremor HVSR
Imaginary part of Green's function
Diffuse Field Assumption (DFA)
Velocity inversion
Sedimentary sequence
Lower reaches of Narmada Valley

ABSTRACT

We propose a rapid and cost-effective Horizontal-to-Vertical Spectral Ratio (HVSR) method that uses microtremors (ambient noise) for mapping intercalated sedimentary sequences with lateral heterogeneity for a depth of about 100 m in Lower reaches of Narmada Valley, western India. The elastic parameters for various units/layers at a given site (1D) were derived theoretically based on HVSR inversion, built on the concepts of Diffuse Field Assumption and retrieval of the imaginary part of Green's function. This approach enables efficient forward calculation, delves into the relationship between the HVSR curve and elastic parameters, and accelerates the inversion process. A site-specific *priori* knowledge gathered during the field visits is further integrated. We successfully derive overall shear wave velocity and density models inferring three sedimentary Units and associated Subunits. The key highlight of this study is successfully distinguishing low-velocity sedimentary Units/Subunits within a sedimentary sequence.

1. Introduction

Knowledge of high and low-velocity units is the key to mapping intercalated sedimentary sequences with lateral heterogeneity. Modelling shear wave velocity without knowing of low-velocity units would lead to errors. Deciphering the low-velocity units at shallow depths is significant in seismic hazard assessment, geotechnical investigations, groundwater exploration (aquifer monitoring), landslide studies, mineral/hydrocarbon exploration, and many more interrelated areas. Several studies have come up that justify the ability of HVSR to decipher comprehensive subsurface layered models [1–9]. However, the studies on velocity inversion as well as vertical and lateral heterogeneity in a terrain help evaluate complexities within the sedimentary basin [10–12].

In the present study, we look forward to distinguishing low-velocity sedimentary layer within a sediment sequence in the Lower reaches of Narmada Valley (LrNV), western India. To achieve the objective, we initially acquire single station (1D) microtremor HVSR followed by inversion adopting the concept of Diffuse Field Assumption (DFA) and retrieval of the imaginary part of Green's function. The DFA uses ambient noise, that includes various types of seismic waves and their components resulting from multiple scattering. The relative power of each seismic state is determined based on the principle of equipartition of energy. As a result, at any point in the medium, the power spectrum is proportional to the imaginary part of Green's function for the source and receiver at the same point [13]. The theory allows computation of the HVSR curve for a region having stratification as an intrinsic property of the medium, linking average energy densities with Green's function in 3D and stems from the properties of diffuse fields [14]. The modelled elastic parameters namely, P-wave velocity (V_p), shear wave velocity (V_s), density (ρ), Poisson's ratio (ν), and layers thickness (h) derived for various units/layers at a given site (1D) are integrated with a site-specific knowledge on sediment sequence gathered during field visits. In the study area, we distinguish three sedimentary Units and associated Subunits, including velocity inversion in a complex sedimentary basin with vertical and lateral heterogeneity at shallow depths.

* Corresponding author.
** Corresponding author.
E-mail addresses: sant.dhananjay-geology@msubaroda.ac.in (D.A. Sant), parvez@csir4pi.in (I.A. Parvez).

https://doi.org/10.1016/j.soildyn.2025.109235
Received 14 September 2024; Received in revised form 21 December 2024; Accepted 15 January 2025

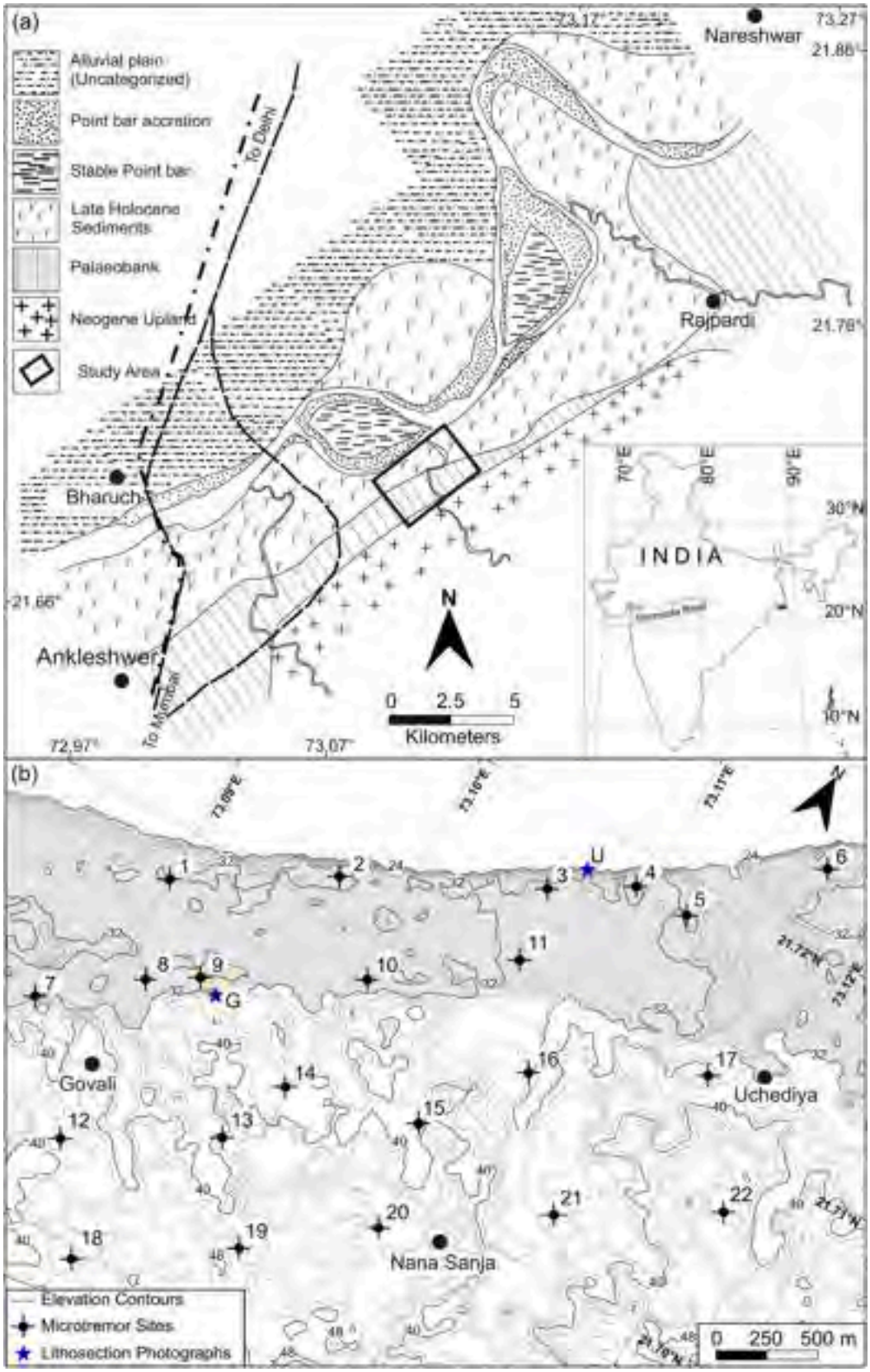

Fig. 1. Location map of the study area: (a) Geology and geomorphology of the lower reaches of the Narmada River [7]. (b) Sites of microtremor measurements within the study area. The shaded area demarcates the Neobank, while the unshaded area represents the Palaeobank. The letters G and U denote the sites near the villages of Govali and Uchediya, respectively (Fig. 2).

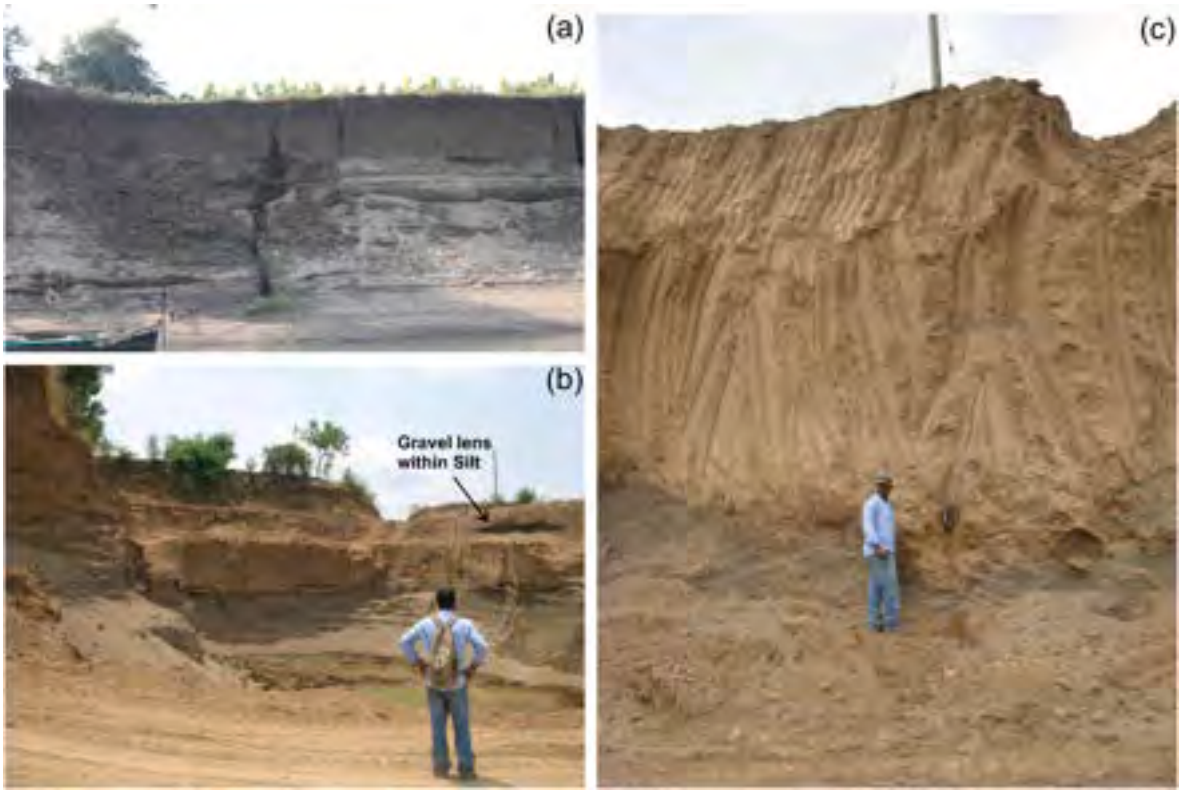

Fig. 2. Field photographs: (a) Sediment sequence exposed along the Narmada River Channel near Uchediya (U in Fig. 1b). The height of the bow is 0.5 m. (b) Sediment sequence exposed near Govali (G in Fig. 1b), showing a gravel lens within silt. (c) Sediment sequence highlighting the silt-gravel interface, east of Govali. In both (b) and (c), the height of the person standing is 1.74 m.

A comprehensive model of the subsurface sediment sequence is built up with the understanding that basin architecture and inherent lateral heterogeneity strongly influence HVSR.

2. Study area

As a case study, we present our findings from the LrNV (Fig. 1a). We select a window of eight square kilometres area northeast of Ankleswar, around villages Govali, Nana Sanja, and Uchediya on the southern bank of the Narmada River situated along the margin of Cambay basin, a major petroliferous basin in western India (Fig. 1a and b) [15,16]. Several researchers have studied fluvial landforms and their intricacy in LrNV using satellites as well as in the field [3,15,17–19]. The only microtremor HVSR studies in LrNV were carried out at 5 km grid intervals to infer Quaternary depocenters [3].

Among the diverse fluvial landforms, a regional ENE-WSW trending scarp is the most prominent. The scarp extends about 65 km from Rajpardi in the east to the mouth of the Narmada River at the Gulf of Cambay. The scarp juxtaposes Palaeobank (older: late Pleistocene terrace) against the Neobank (500 years old) [20]. About 4.3 Km of scarp is exposed within the study area (Fig. 1b). The present Narmada Riverbank (neobank) is about 8 m higher than the channel, whereas the Palaeobank stands at about 10 m–14 m above the neobank. The exposed neobank sediment sequence dominates with silt and sand (Fig. 2a), whereas the Palaeobank sediment sequence comprises silt, sand, and gravel. Lenticular bodies of sand and gravel are commonly encountered in the study area (Fig. 2b).

3. Methodology

3.1. Data acquisition

We carried out single-station microtremor measurements using a triaxial seismometer (LE-3D Lennartz-5s period) and a City Shark-II data acquisition system at a sampling rate of 100 Hz. Microtremor measurements were taken for 40 min at each site in March 2009. The measurement duration for data acquisition is about three times more than recommended by the SESAME Guidelines [21]. Twenty-two sites were selected, covering an eight-square-kilometer area for microtremor measurements such that Palaeobank (Sites 1 to 11) and Neobank (Sites 12 to 22) are likewise represented. The sites fall apart by about 500 m (Fig. 1b).

3.2. Data analysis

The microtremor data procured from the field was processed using "Geopsy" software (http://www.geopsy.org) [21,22] to obtain the HVSR curve. The shape of the HVSR curve was further studied together with single-component spectra. HVSR inversion was carried out using HV-Inv (an open-source MATLAB 2015a-based GUI; https://w3.ual.es/GruposInv/hv-inv/) [23,24] (Fig. 3).

3.2.1. HVSR analysis

Three-component waveform data were manually filtered by removing the windows mixed with momentary ambiguous signals (Fig. 4). The persistent and transient signals were further removed using an anti-triggering algorithm. Smoothening of the HVSR curve is carried out using Cosine tapering and Konno Ohmachi filter with a bandwidth coefficient value of 40 [25].

In the present study, we adopt a bandwidth range from 1 Hz to 20 Hz, considering 50 s long-time windows with 5 % overlap. We obtain Fourier amplitude spectra for each component (East-West, North-South, and Vertical). H/V ratio was taken considering horizontal components as total horizontal energy by combining E-W and N-S components.

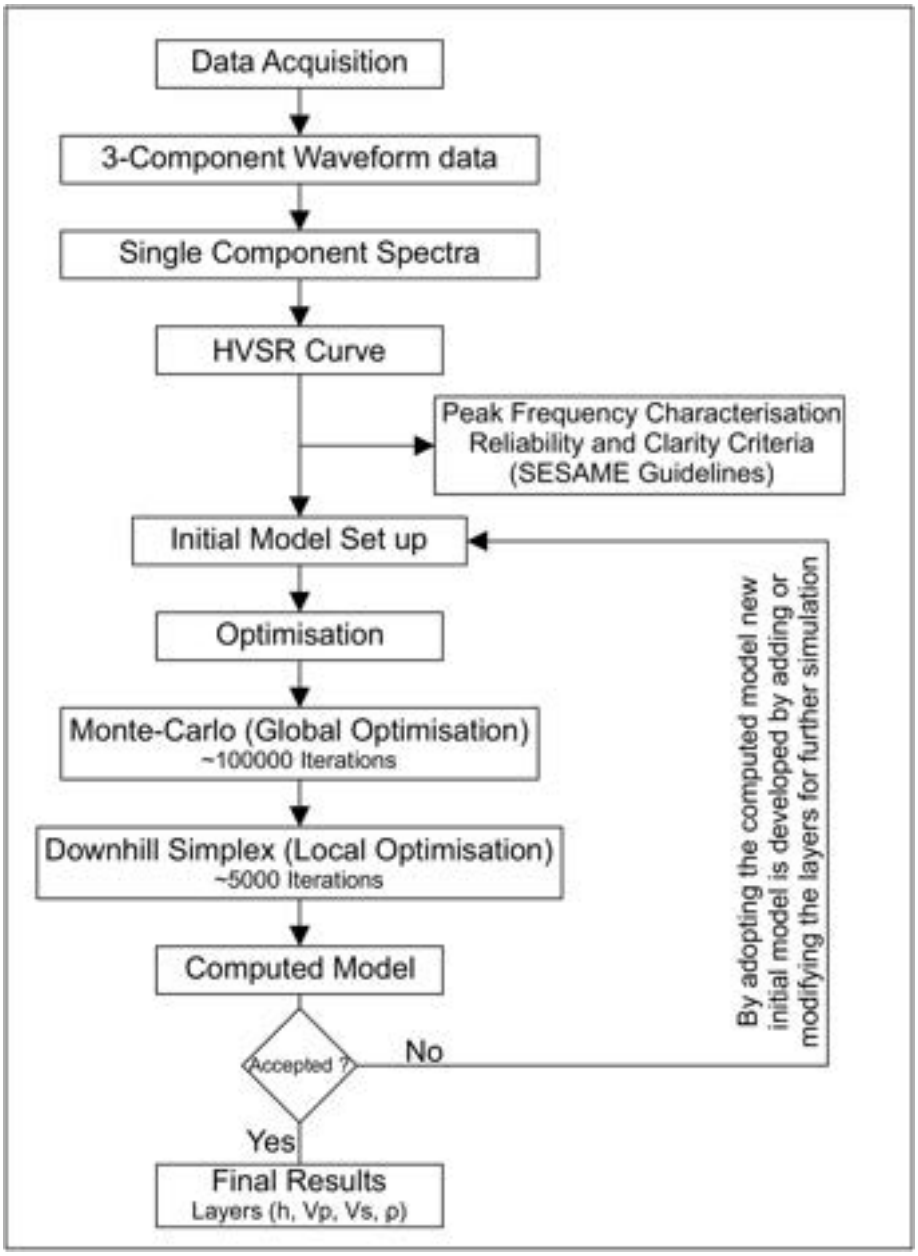

Fig. 3. Flow chart showing methodology adopted for data analysis.

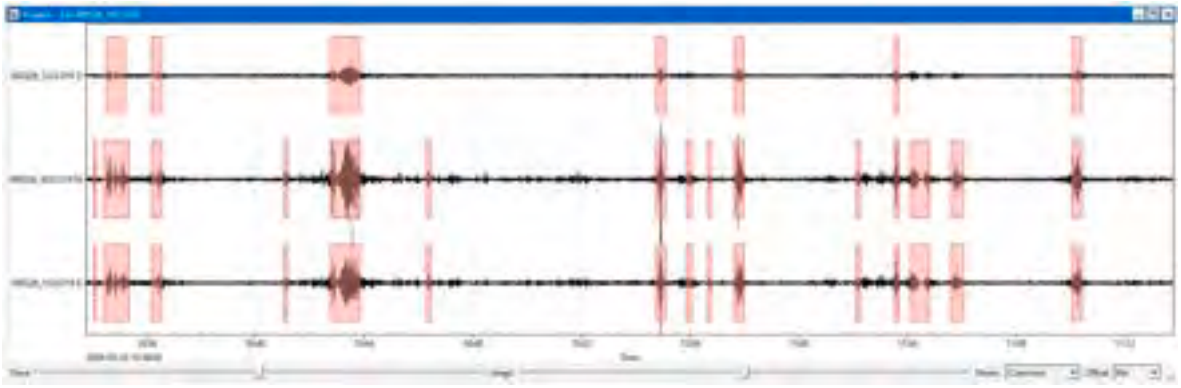

Fig. 4. Three-component waveform data for Site 17. The waveform exemplifies manual filtering by removing the windows mixed with momentary ambiguous signals.

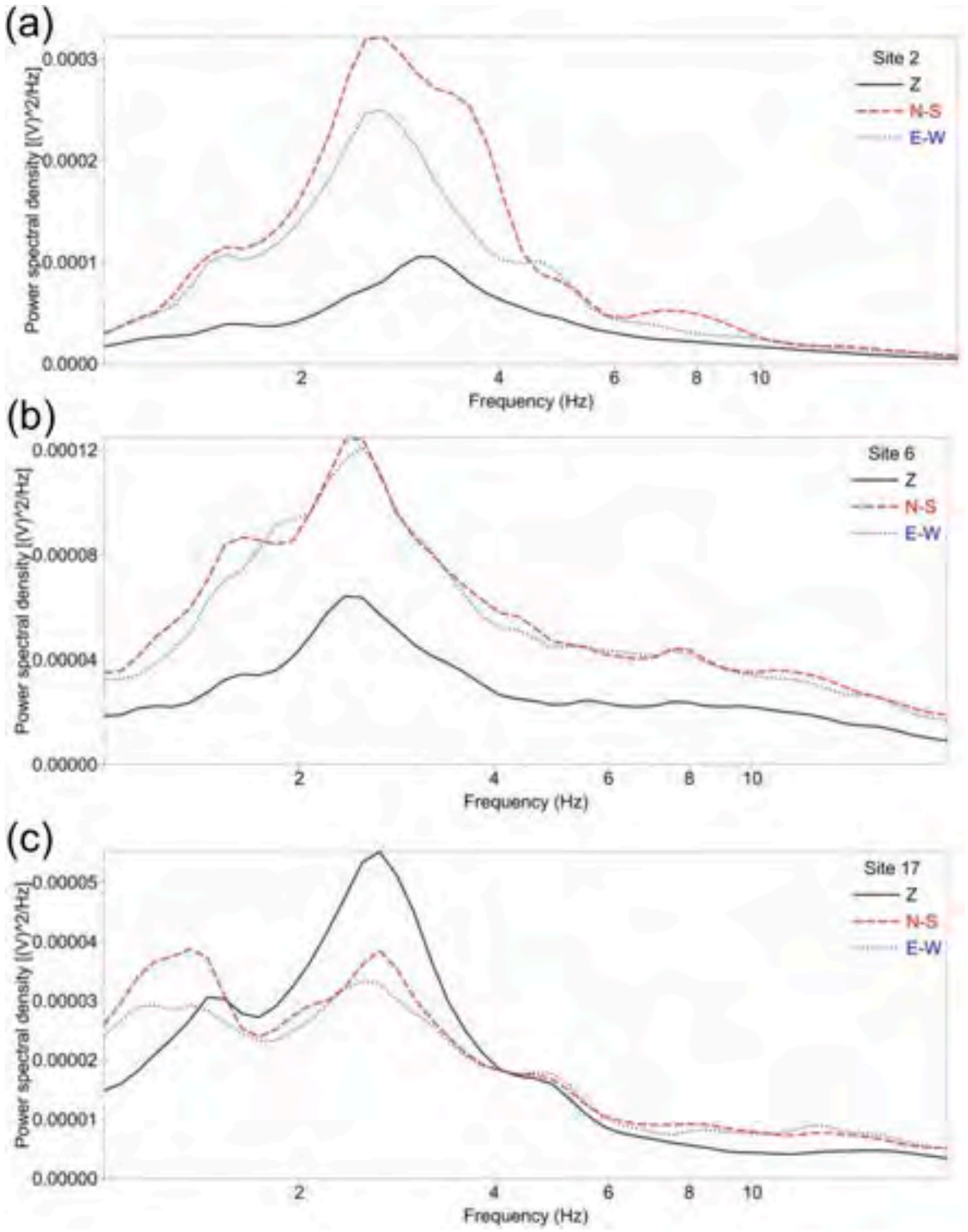

Fig. 5. Single component Fourier spectra for three scenarios (a) Scenario 1, a significant difference between N-S and E-W components (Site 2); (b) Scenario 2, Vertical component less than the Horizontal component (Site 6); (c) Scenario 3, Vertical component greater than the Horizontal component (Site 17). Single-component Fourier spectra for all sites are compiled in Annex 1.

$$\left[\frac{H}{V}\right](f) = \frac{\sqrt[2]{E_N^2(f) + E_E^2(f)}}{E_V(f)}$$

Here $E_N(f)$, $E_E(f)$ and $E_V(f)$ are spectral energy densities of the N-S, E-W and Vertical components respectively.

The general amplitude and shape of the HVSR curve depend on V_p, V_s, ρ, ν and h instead of subsoil and source configurations [26]. The shape of the HVSR curve is investigated in relation to the single-component power spectral density (Annex 1). We observe three scenarios, (1) the difference between N-S and E-W components (Fig. 5a), (2) the Vertical component less than the Horizontal component (Fig. 5b), (3) the Vertical component greater than the Horizontal component (Fig. 5c). Scenario 1 is indicative of subsurface lateral heterogeneity and basin morphology [27]; Scenario 2, distinguishes

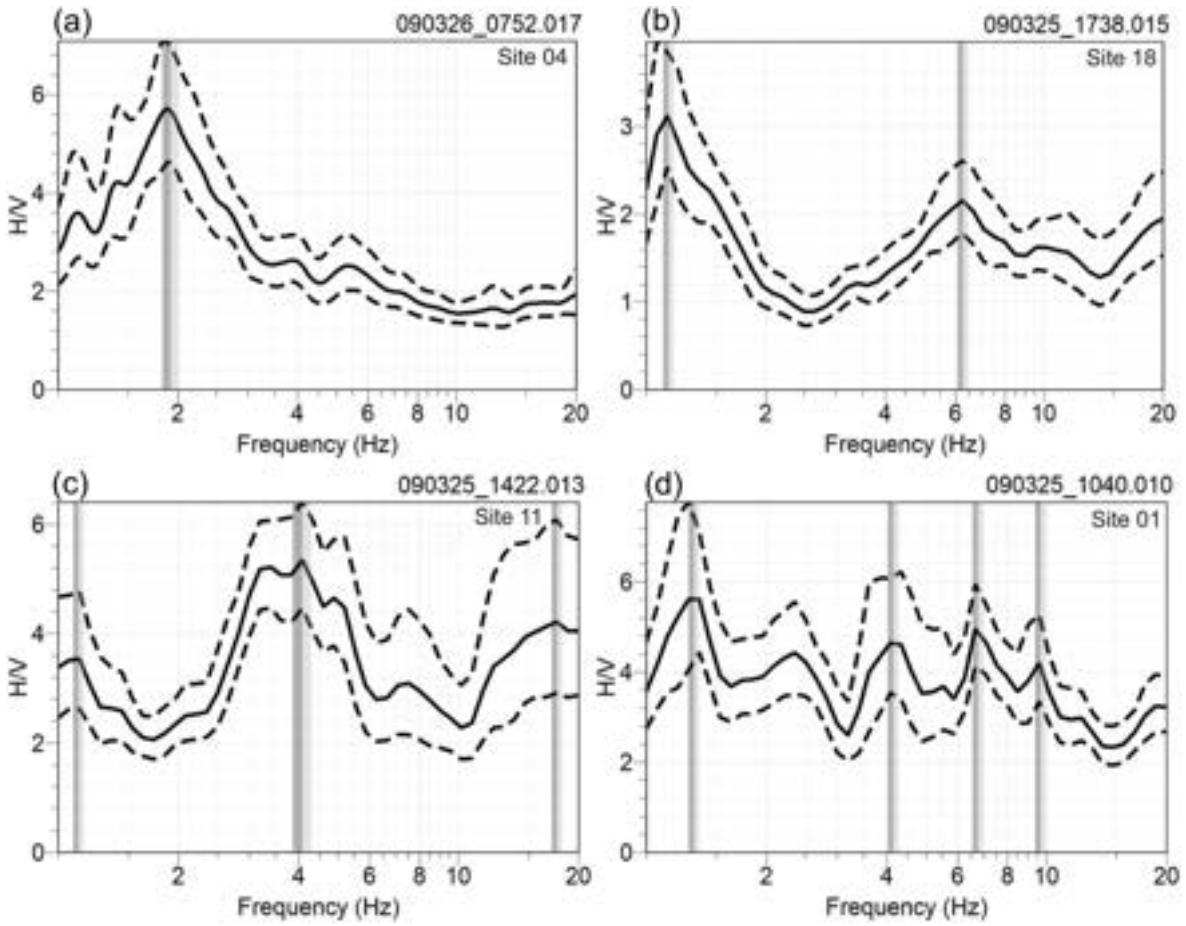

Fig. 6. Representative HVSR curves showing peak resonating frequency (a) single peak, Site 4 (b) two peaks, Site 18 (c) three peaks, Site 11 and (d) four peaks Site 1. The HVSR curve for all sites is compiled in Annex 2.

prominent resonant frequency peaks along the HVSR curve [21]; whereas in scenario 3, the values of HVSR fall <1 [11,12]. Such variability accounts for basin morphology and complexity in the sedimentary sequence [28–30].

3.2.2. HVSR and DFA

In a diffuse field, the imaginary part of Green's function can be retrieved from the average cross-correlations of the displacements and thereby energy. In cases where the source and receiver are at a single point, the directional energy density $E_i(x,\omega)$ at point x of the same component, is directly proportional to the imaginary part of Green's function (Im $[G_{ii}(x,x;\omega)]$) [14].

$$E_i(x,\omega) \propto \text{Im}\,[G_{ii}(x,x;\omega)]$$

The ratio H/V can be experimentally computed in the frequency domain through autocorrelations of the displacement signals expressed as the imaginary part of Green's function that determines the synthetic HVSR curve.

$$\frac{H}{V}(x,\omega) = \sqrt{\frac{\text{Im}\,[G_{11}(x,x;\omega)] + \text{Im}\,[G_{22}(x,x;\omega)]}{\text{Im}\,[G_{33}(x,x;\omega)]}}$$

Here 1, 2 and 3 represent three components, namely E-W, N-S and Vertical, respectively. It is assumed that the medium is homogeneous, isotropic and elastic with V_p, V_s, δ and h having layered half-space and unbounded interfaces [24].

3.2.3. HVSR inversion

We reconstruct a comparable synthetic HVSR curve through inversion providing an initial model. The non-uniqueness in HVSR inversion can be minimised with a prior understanding of sediment sequence that ameliorates achieving a comprehensive model reducing processing time. The number of layers within a model is decided based on the compilation of peak resonance frequencies from all sites that qualify for the reliability (all three) and clarity (minimum 4 out of 6) criteria provided by the SESAME Guidelines [21]. The elastic parameter ranges for each layer were based on the recommended values for sediment type, as outlined in previous studies [31–33]. The adopted parameter ranges were marginally modified considering the characteristic sedimentology of local sediment type. The range of Poisson's ratio (ν) considered in the present study is 0.25–0.40. The interrelationship between elastic parameters for different layers is crucial for understanding their influence over inversion results [34].

The best fit between the measured HVSR curve and the synthetic curve is quantified by misfit value [24]. The misfit (Γ_{HV}) in this study is defined as the:

$$\Gamma_{HV} = \sum_{i=1}^{n} \frac{\left(HV(\omega_i) - HV_{syn}(\omega_i)\right)^2}{\sigma_{HV}^2(\omega_i)}$$

Here, HV denotes the HVSR calculated for a particular site. HV_{syn} signifies the synthetic HVSR corresponding to the n^{th} model, σ_{HV} refers to the standard deviation of the HVSR curve, and ω_i denotes the i^{th} frequency point within this n^{th} model's curve.

3.2.4. Velocity inversion

The concept of resolving velocity inversion in a sedimentary terrain using ambient noise was introduced by Di Giacomo et al. [10].

Table 1
Peak resonant frequencies (f) and their Amplitude (A_f) are tabulated for all 22 sites. The selected frequencies qualify for the reliability (all three) and clarity (minimum 4 out of 6) criteria provided by the SESAME Guidelines [21].

Site	f	A_f	Clarity	f	A_f	Clarity	f	A_f	Clarity
Neobank									
1	1.29	5.27	4	4.01	4.16	4	9.47	3.97	5
1				6.79	4.47	5			
2				2.51	5.91	5			
3	1.96	5.45	6						
4	1.96	5.53	4						
5				2.32	5.15	5	7.58	3.04	4
6	1.72	4.34	4						
7				4.35	5.62	4	14.44	5.76	4
8	1.14	3.13	5						
9				3.86	3.87	6			
10				3.21	5.50	6	18.36	3.33	5
11	1.11	3.57	4	3.99	5.47	5	17.83	4.13	4
Paleobank									
12	1.15	4.38	5	5.27	3.13	4			
13	1.10	3.17	4	5.96	2.28	4	13.22	2.62	4
14							10.68	4.30	5
15	1.13	3.13	5	6.16	4.80	4	13.07	2.27	4
16	1.14	3.97	4	3.74	6.97	6			
17	1.15	2.62	5				12.41	3.29	4
18	1.13	3.17	4	6.26	2.13	5			
19	1.17	4.58	5	6.03	3.37	5			
20	1.12	3.44	4				9.38	4.66	6
21	1.12	3.44	4	4.64	3.95	6			
22	1.10	2.72	4	6.87	3.14	4	17.78	2.62	4

Microtremor measurements conducted along stiff paving, compared to the underlying shallow subsoil, were studied in various contexts. These studies suggested that velocity inversion could be identified at shallow depths [11]. Studies on ambient noise and earthquake recordings in northern Italy have focused on characterising velocity inversion along with the vertical and lateral heterogeneity in local geology [12].

García-Jerez et al. [23] and Piña-Flores et al. [24,35] developed a MATLAB 2015a algorithm (HV-Inv) based on DFA and retrieval of the imaginary part of Green's function enabling the user to model velocity inversion if present. The phenomenology of HVSR curves is a primary reflection of scenarios 2 and 3 (section 3.2.1). Under scenario 2, where the vertical component is less than the horizontal component, one sees a prominent resonant frequency peak along the HVSR curve reflecting a positive velocity gradient. Whereas under scenario 3, where the vertical component is greater than the horizontal component, the HVSR curve shows a wide trough below an amplitude 1 over a wide frequency range. Scenario 3 complements velocity inversion however, velocity inversion is unlikely under scenario 2. We propose, therefore, that in natural conditions where one sees the possibility of intercalated sequence (intercalation between silt-gravel- sand or silt-gravel- silt or gravel-sand-gravel), there are all chances of encountering velocity inversion.

4. Results and discussion

The single-component Fourier spectral curves are investigated in accordance with HVSR. We observe a significant variation within the

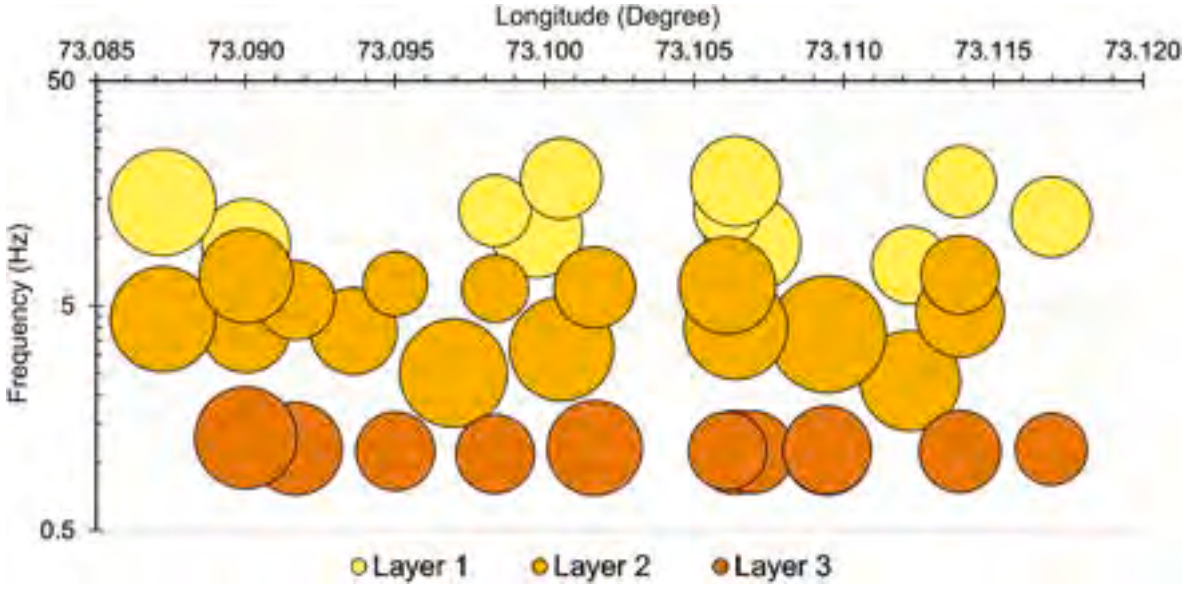

Fig. 7. Bubble diagram showing variation in the resonant frequency of all 22 sites. The bubbles' diameter captures the resonant frequency amplitude at ≥1 sigma level. The bubble diagram highlights the presence of three layers. The frequency >7 Hz, Layer 1; the frequency range between 7 Hz and 2 Hz, Layer 2; and the frequency <2 Hz, Layer 3.

Table 2
The initial model for HVSR inversion. The number of layers adopted was decided based on the compilation of peak resonance frequencies from all 22 sites (Table 1 and Fig. 7) whereas the ranges of elastic parameters for each layer were adopted about the prescribed ranges from general elastic parameters for sedimentary layers [31–33]. The adopted parameter ranges were marginally modified considering the characteristic sedimentology of local sediment type.

Layers	h (m)	V_P (m/s)	V_S (m/s)	ρ (kg/m^3)	ν
L1	0–10	160–600	80–300	1100–1800	0.25–0.4
L2	10–75	700–2000	350–1000	1800–2500	
Half space	0	2000–5000	1000–2500	2200–2700	

power spectral densities of horizontal components at Sites 1 and 16. At Site 1 it imparts multiple peaks between 2 Hz and 10 Hz, whereas a broad peak is observed between 3 Hz and 8 Hz at Site 16 in the respective HVSR curve. However, the marginal difference within power spectral densities of horizontal components subdues the HVSR peak. Sites 1 to 11 except Site 8 exhibit a lower vertical component amplitude compared to the horizontal component characterising a peak along respective HVSR curves. Conversely, Sites 12 to 22 except Site 21 demonstrate a lower amplitude of the horizontal components, compared to the vertical component (Annex 1) resulting in a trough in the HVSR curve with an amplitude below 1 within frequency ranges from 1 Hz to 6 Hz (Annex 2a). The relationships between horizontal and vertical components capture the expected control of basin morphology and lateral heterogeneity in the study area [15–17].

The HVSR curves obtained for the sites show both single and multiple resonant frequency peaks. Sites 2, 3, 4, 6, 8, 9, and 14 exhibit single peak (e.g., Fig. 6a); Sites 5, 7, 10, 12, 16, 17, 18, 19, 20, and 21 displays two peaks (e.g., Fig. 6b); Sites 11, 12, 15 and 22 reveal three peaks (e.g., Fig. 6c); whereas site 1 unveil four peaks (e.g., Fig. 6d). The resonant frequency peaks identified along HVSR curve satisfies all reliability and clarity (four out of six) criteria set by SESAME guidelines [21].

Compilation of the HVSR results for all 22 sites recommends three prominent peak resonant frequency ranges viz., greater than 7 Hz, 7 Hz–2 Hz and less than 2 Hz (Table 1). The frequency ranges highlighted in Fig. 7 draw attention to the presence of at least three distinct impedance contrasts within the subsurface sediment sequence in the study area. On this basis, we conceptualise a subsurface three-layered initial model to provide the conditions most likely for successful inversion (Table 2). Appropriate ranges of ρ *and* V_s were adopted and marginally modified considering prior knowledge of local sediment. HVSR inversion is achieved using Monte-Carlo and Downhill Simplex algorithm for optimisation till we achieve minimum misfit (Fig. 3). The layers are added/modified during the progression of analysis to provide additional freedom in the model, bringing down the misfit [36]. At certain sites where we observe increasing trend of HVSR curve at 20 Hz implies possibile peak above 20 Hz (shallow depths). To satisfy this condition during HVSR inversion, we add a layer close to 20 Hz to lower the misfit.

Out of 22 sites, the misfits for nine sites are less than or equal to 1.5; for eight sites, misfits range from 1.5 to 3; and for six sites, misfits below 5. The HVSR inversion models advocate for a 5-layer model at fifteen sites; a 4-layer model at sites 5, 9 and 10; a 6-layer model at sites 1, 14, and 16; and a 3-layer model at site 8 inclusive of half space.

A strong correlation is evident between $V_p - V_s$ (Fig. 8a) and $V_s - \rho$ (Fig. 8b) with R^2 values of 0.98 and 0.94 respectively, indicating that the material has consistent and predictable elastic properties. The unit-wise plot of the $V_s - \rho$ (Fig. 8c) distinctly differentiates three Units. Unit 1, V_s ranging from 80 m/s to 305 m/s (Fig. 9a); Unit 2, V_s ranging from 340 m/s to 945 m/s (Fig. 9b); and Unit 3, V_s ranging from 1000 m/s to 2200

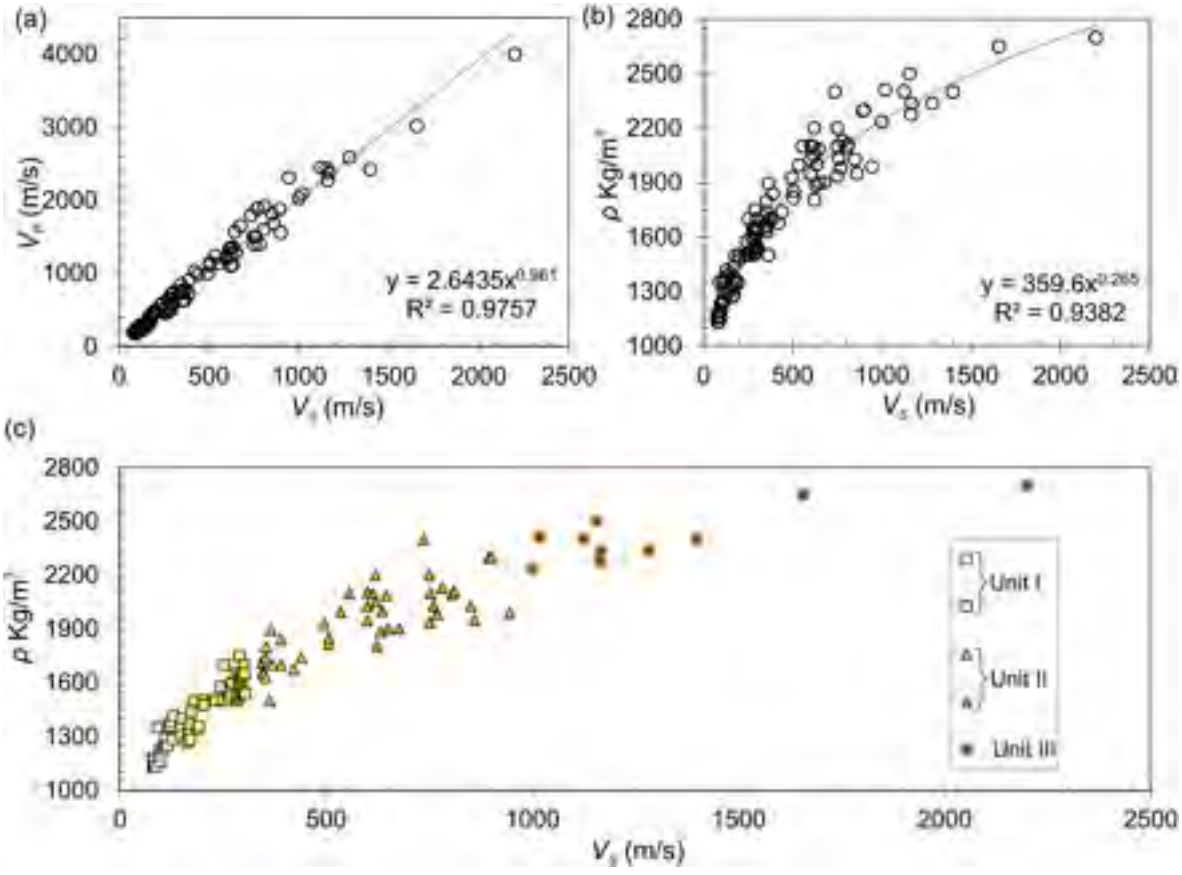

Fig. 8. (a) Scatter plots of V_s *against* V_p. (b) Scatter plots of V_s against ρ. (c) Scatter plot V_s against ρ capturing clusters of three distinct Units and associated Subunits. The data incorporates modelled values of V_p, V_s, and ρ from all 22 sites.

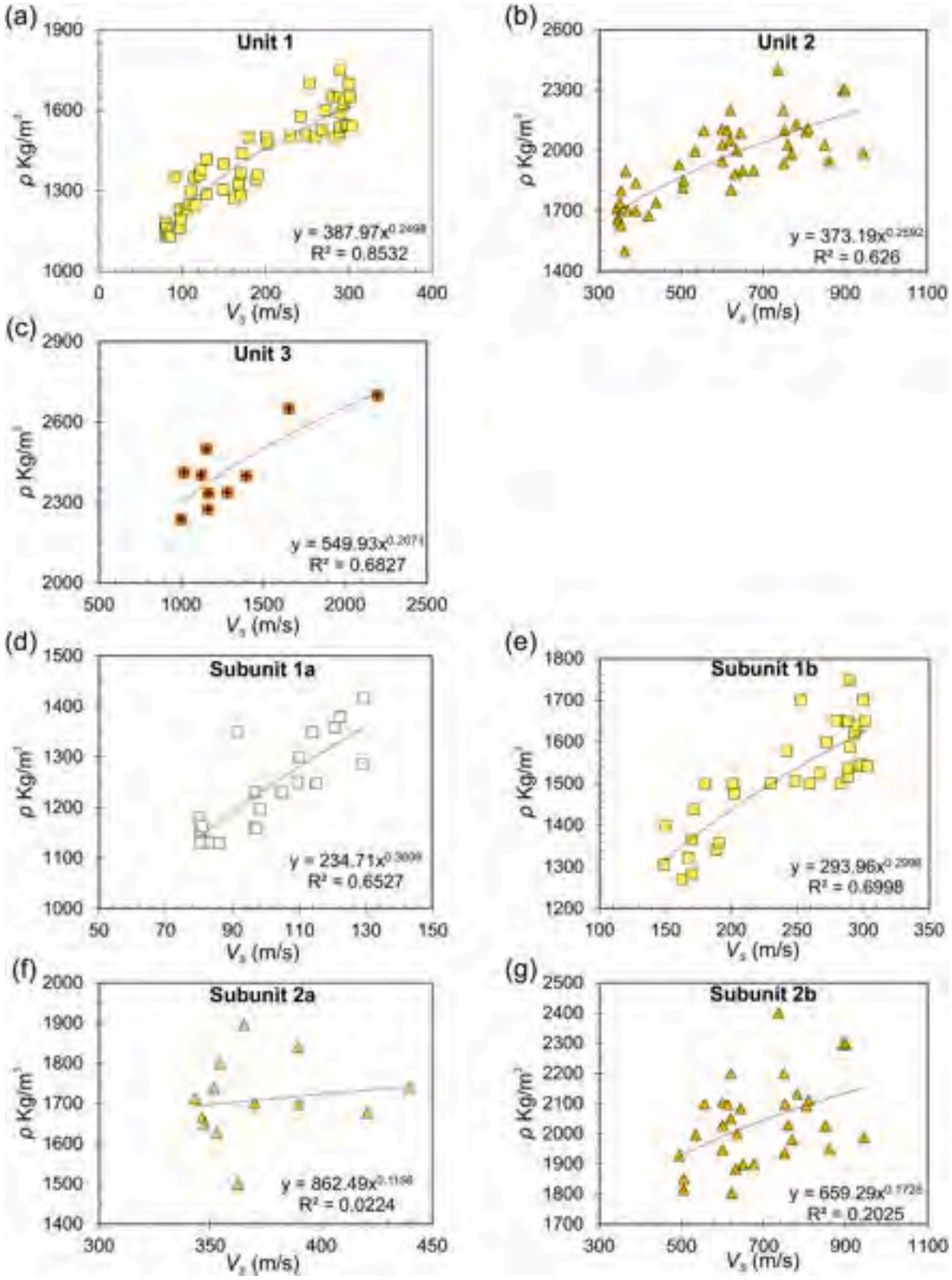

Fig. 9. Scatter plots of modelled V_s against ρ for (a) Unit 1 (silt + fine sand), (b) Unit 2 (sand + gravel), (c) Unit 3 (Neogene sedimentary rocks). (d) Subunit 1a (silt), (e) Subunit 1b (fine sand), (f) Subunit 2a (sand), and (g) Subunit 2b (coarse sand + gravel). The inference on sediment type is based on results compiled in Fig. 8c with information gathered during field visits. The lower R^2 values for Subunits 2a (f) and Subunit 2b (g) are likely due to the nonlinear relationship between variability of seismic energy due to reflection, refraction, scattering, and absorption with different sediment types having variable porosity and compaction.

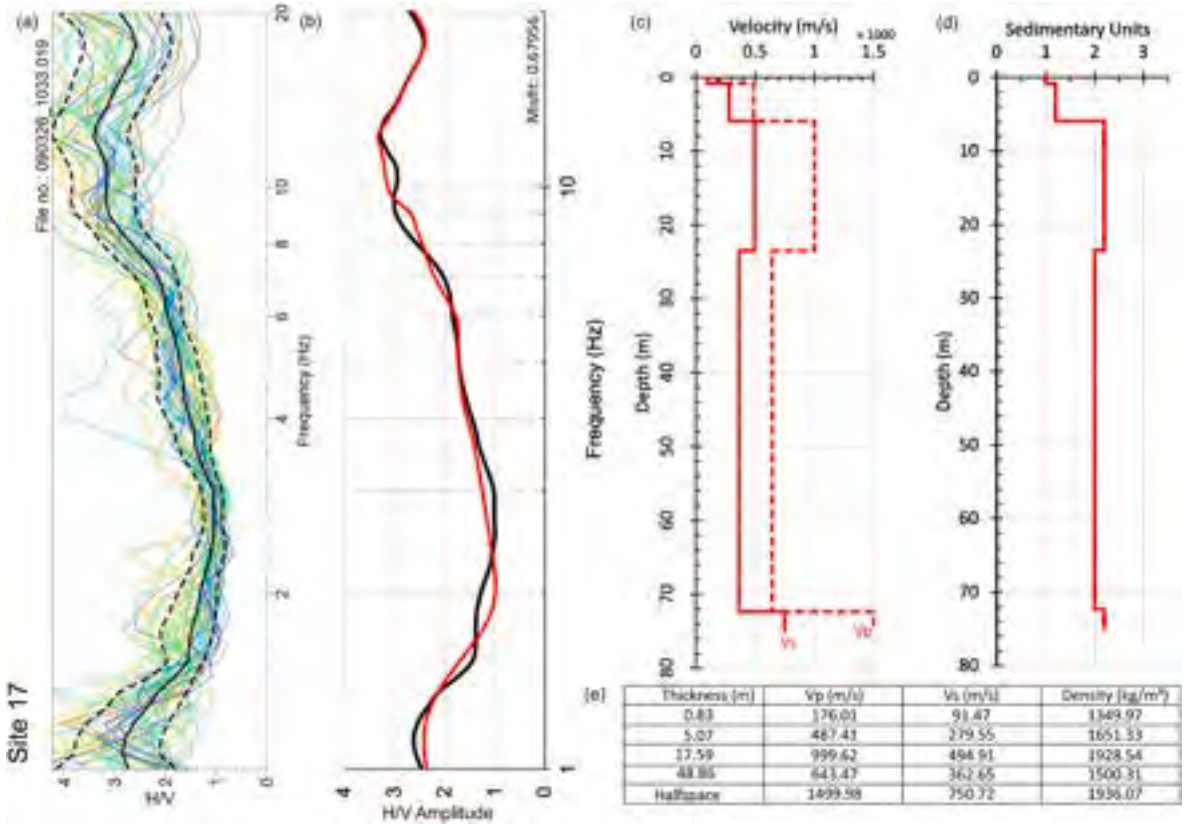

Fig. 10. Results of microtremor HVSR studies for Site 17. (a) Microtremor HVSR curve obtained from Geopsy [21,22] (b) The black colour curve represents the measured HVSR curve for the site. The red colour curve represents synthetic HVSR obtained through inversion using Hv-Inv [23]. (c) The plot illustrates the variation of modelled V_p (dashed line) and V_s (solid line) with depth at the site (d) The plot shows inferred sedimentary units along the depth. The inference on sediment type is based on integrating results compiled in Fig. 8c with information gathered during field visits. The x-axis represents sedimentary units where, 1, 2, and 3 represent Unit 1- silt + fine sand, Unit 2 – sand + gravel, and Unit 3 – Neogene sedimentary rocks respectively. (e) Elastic parameters (Thickness, V_p, V_s, and Density) for sediment layers at a site were obtained through HVSR inversion. Similar results for all 22 sites are compiled in Annex 2. (For interpretation of the references to colour in this figure legend, the reader is referred to the Web version of this article.)

m/s (Fig. 9c). Unit 1 and Unit 2 are further subdivided into two Subunits each. Unit 1a, V_s ranging from 80 m/s to 130 m/s (Fig. 9d); Unit 1b, V_s ranging from 145 m/s to 305 m/s (Fig. 9e); Unit 2a, V_s ranging from 340 m/s to 440 m/s (Fig. 9f); Unit 2b, V_s ranging from 490 m/s to 945 m/s (Fig. 9g). The lower R^2 value of $V_s - \rho$ relationship for Subunits 2a and 2b (Fig. 9f and g) apprehends a nonlinear relationship between variability of seismic energy due to reflection, refraction, scattering, and absorption with different sediment types having variable porosity and compaction.

For a meaningful interpretation, the unit-wise division procured from the HVSR inversion was compared with the local field-based records on sedimentary sequence. The Neogene sedimentary rocks (Unit 3) form the base of the Quaternary sediment sequence (Unit 2 and 1). Sand + gravel (Unit 2) overlay Unit 3. Sand (Subunit 2a) usually lay above the coarse sand + gravels (Subunit 2b) however, lenses of Subunit 2a within Subunit 2b are common. Finally, Unit 1 (fine sand + silt) caps the sediment sequence. The Subunit 1b (fine sand + silt) shows undulation along the interface with underlying Unit 2. Silt (Subunit 1a) blankets the sediment sequence in the study area (Fig. 2).

The compilation of the HVSR curves, results of HVSR inversion, and inferred sedimentary units for representative site (Site 17) are compiled (Fig. 10). The results of all sites are presented in Annex 2. We observe a positive velocity gradient along depth at rows 1 and 2 over the Neobank. Sites 12 to 22 on Palaeobank set apart sediment units showing velocity inversion compared to overlaying and underlying units. The HVSR curve for these sites shows a prominent trough below amplitude 1 between frequencies 1 Hz and 6 Hz. An inclusive terrain model is attempted by plotting the depth of sedimentary units deciphered based on $V_s - \rho$ relationship (Fig. 8c) for Sites 1 to 6 (Row 1), Sites 7 to 11 (Row 2); Sites 12 to 17 (Row 3) and Sites 18 to 22 (Row 4). We connect interfaces of units and subunits distinguished at each site to build cross-sections along rows 1 to 4 (Fig. 11). The terrain model suggests the silt unit caps the sedimentary sequence, followed by fine sand + silt, sand and coarse sand + gravel, while the Neogene sedimentary rocks form the base. The Neogene sedimentary rocks are mapped underneath Sites 2, 7, 10, 11, 14, 16, 19 and 21. A low-velocity sedimentary units of coarse sand (Subunit 2a) are distinctly set apart in the sequence within coarse sand + gravel (Subunit 2b). The common occurrence of lensoidal bodies in the exposed sediment sequences gives good reason for extrapolating Subunit 2a (sand) as a lensoidal shape at Sites 12, 13, 14, and 17. Similarly, fine sand + silt (Unit 1b) within coarse sand + gravel (Subunit 2b) at Sites 16 and 18 marks a low-velocity sediment unit and a high-density Subunit 2b is further mapped within Subunit 1b at Sites 15 and 20.

5. Conclusion

We apply the microtremor HVSR and HVSR inversion technique to model subsurface velocity structure up to 100 m in the Quaternary sedimentary basin, LrNV, western India. The microtremor measurements were carried out on 22 sites. Each site was analysed to estimate the 1-D elastic parameters for various units/layers based on concepts of DFA and the imaginary part of Green's function retrieval. The velocity and density relationships were worked out suggesting the presence of three-layered models related to three sedimentary units. Our analysis yields velocity inversion highlighting strong heterogeneity in the shallow subsurface. Unit-wise 1-D velocity model along Rows 1 to 4 is

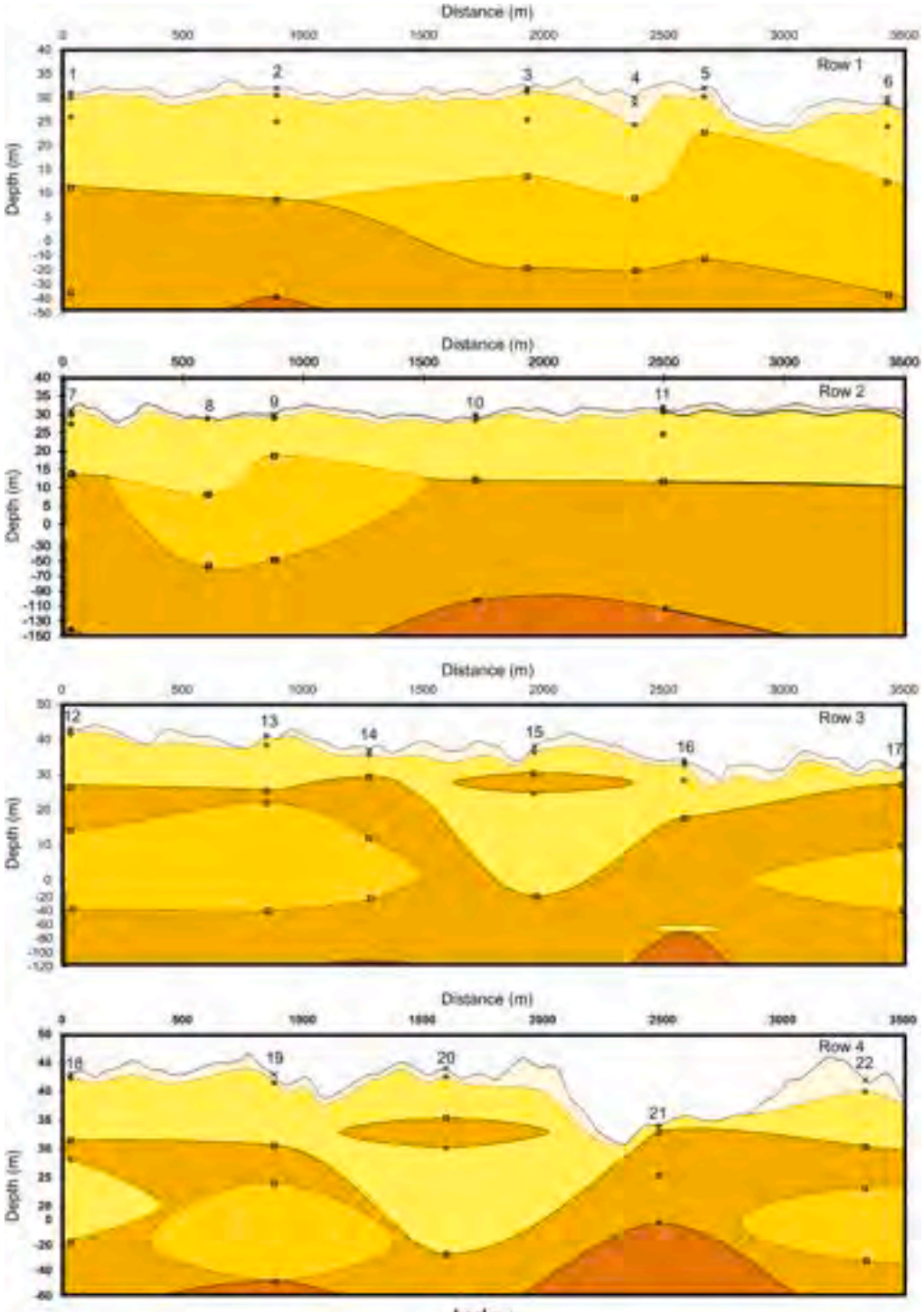

Index

Unit	Subunit	V_p (m/s)	V_s (m/s)	ρ (kg/m^3)
Unit 1	Subunit 1a	175 - 300	80 - 130	1130 - 1420
	Subunit 1b	265 - 745	145 - 305	1260 - 1750
Unit 2	Subunit 2a	625 - 1035	340 - 440	1250 - 1900
	Subunit 2b	990 - 2310	490 - 945	1800 - 2500
Unit 3		2030 - 2700	1000 - 2200	2230 - 2700

(caption on next page)

Fig. 11. Cross-section extrapolating sedimentary units connecting sites along Rows 1 to 4. The sediment units are inferred by integrating results compiled in Fig. 8c with information gathered during field visits. The numbers (1–22) on the profile represent the site of microtremor measurements. Row 1 and Row 2 show positive velocity gradients whereas Row 3 and Row 4 highlight lenses of low-velocity units within sedimentary sequence. Unit 1, silt + fine sand; Subunit 1a, silt; Subunit 1b, fine sand; Unit 2, sand + gravel, Subunit 2a, sand; Subunit 2b, coarse sand + gravel; and Unit 3, Neogene sedimentary rocks.

attempted. Rows 1 and 2 characterise the Neobank sequence whereas Rows 3 and 4 characterise the Palaeobank sequence. The Neobank sequence shows a positive velocity gradient whereas the Palaeobank sequence highlights the occurrence of low-velocity units. Cross-sections connecting sites are extrapolated inferring sediment sequence along rows. Further work in sedimentary basins is sure to benefit in understanding the intricacies of the HVSR curve with terrain.

CRediT authorship contribution statement

Dhananjay A. Sant: Writing – review & editing, Writing – original draft, Visualization, Validation, Supervision, Software, Resources, Project administration, Methodology, Investigation, Funding acquisition, Formal analysis, Data curation, Conceptualization. **Gunjankumar K. Makwana:** Writing – review & editing, Writing – original draft, Visualization, Validation, Software, Methodology, Formal analysis. **Prabhin Sukumaran:** Writing – review & editing, Validation, Resources, Project administration, Investigation, Funding acquisition, Data curation, Conceptualization. **Imtiyaz A. Parvez:** Writing – review & editing, Validation, Supervision, Software, Resources, Methodology, Formal analysis, Data curation. **Govindan Rangarajan:** Writing – review & editing, Validation, Supervision, Resources, Funding acquisition, Formal analysis. **K. Krishnan:** Writing – review & editing, Supervision, Resources, Project administration, Investigation, Funding acquisition.

Declaration of competing interest

The authors declare the following financial interests/personal relationships which may be considered as potential competing interests: Prof. Dhananjay A. Sant reports financial support was provided by India Ministry of Science & Technology Department of Science and Technology. If there are other authors, they declare that they have no known competing financial interests or personal relationships that could have appeared to influence the work reported in this paper.

Acknowledgements

The authors thank the Department of Science and Technology, Shallow Sub-surface Science program – Narmada Window WINDOW/P 6) for the financial support through a project grant. We thank Dr Jose Pina-Flores, Department of Geophysical Engineering, Universidad Nacional Autónoma de México, for constructive discussion during data processing. We thank Professor Atul Joshi, Head of the Department of Geology and Dean, Faculty of Science, Prof. H. R. Kataria, for their constant support and encouragement during data processing. We thank Prof. P. K. Mehta, Head, of the Department of Computer Application, for extending the computing facility. I.A.P. thanks the Director of CSIR-Fourth Paradigm Institute for her support and encouragement.

Appendix A. Supplementary data

Supplementary data to this article can be found online at https://doi.org/10.1016/j.soildyn.2025.109235.

Data availability

Data will be made available on request.

References

[1] Ibs-von Seht M, Wohlenberg J. Microtremor measurements used to map thickness of soft sediments. Bull Seismol Soc Am 1999;89:250–9. https://doi.org/10.1785/BSSA0890010250.
[2] Parolai S, Bormann P, Milkereit C. New relationships between vs, thickness of sediments, and resonance frequency calculated by the H/V ratio of seismic noise for the cologne area (Germany). Bull Seismol Soc Am 2002;92:2521–7. https://doi.org/10.1785/0120010248.
[3] Sukumaran P, Parvez IA, Sant DA, Rangarajan G, Krishnan K. Profiling of late Tertiary-early Quaternary surface in the lower reaches of Narmada valley using microtremors. J Asian Earth Sci 2011;41:325–34. https://doi.org/10.1016/j.jseaes.2011.02.011.
[4] Spica Z, Caudron C, Perton M, Lecocq T, Camelbeeck T, Legrand D, et al. Velocity models and site effects at Kawah Ijen volcano and Ijen caldera (Indonesia) determined from ambient noise cross-correlations and directional energy density spectral ratios. J Volcanol Geoth Res 2015;302:173–89. https://doi.org/10.1016/j.jvolgeores.2015.06.016.
[5] Joshi AU, Sant DA, Parvez IA, Rangarajan G, Limaye MA, Mukherjee S, et al. Subsurface profiling of granite pluton using microtremor method: southern Aravalli, Gujarat, India. Int J Earth Sci 2018;107:191–201. https://doi.org/10.1007/s00531-017-1482-9.
[6] Sant DA, Parvez IA, Rangarajan G, Patel SJ, Bhatt MN, Sanoop Salam TA. Subsurface profiling along Banni Plains and bounding faults, Kachchh, Western India using microtremors method. J Asian Earth Sci 2017;146:326–36. https://doi.org/10.1016/j.jseaes.2017.06.002.
[7] Sant DA, Parvez IA, Rangarajan G, Patel SJ, Sanoop Salam TA, Bhatt MN. Subsurface imaging of brown coal bearing Tertiary sedimentaries - deccan Trap interface using microtremor method. J Appl Geophy 2018;159:362–73. https://doi.org/10.1016/j.jappgeo.2018.09.008.
[8] Perton M, Spica Z, Caudron C. Inversion of the horizontal-to-vertical spectral ratio in presence of strong lateral heterogeneity. Geophys J Int 2018;212:930–41. https://doi.org/10.1093/gji/ggx458.
[9] Perton M, Spica ZJ, Clayton RW, Beroza GC. Shear wave structure of a transect of the Los Angeles basin from multimode surface waves and H/V spectral ratio analysis. Geophys J Int 2020;220:415–27. https://doi.org/10.1093/gji/ggz458.
[10] Di Giacomo D, Gallipoli MR, Mucciarelli M, Parolai S, Richwalski SM. Analysis and modeling of HVSR in the presence of a velocity inversion: the case of Venosa, Italy. Bull Seismol Soc Am 2005;95:2364–72. https://doi.org/10.1785/0120040242.
[11] Castellaro S, Mulargia F. The effect of velocity inversions on H/V. Pure. Appl Geophys 2009;166:567–92. https://doi.org/10.1007/s00024-009-0474-5.
[12] Panzera F, Lombardo G, Monaco C, Di Stefano A. Seismic site effects observed on sediments and basaltic lavas outcropping in a test site of Catania, Italy. Nat Hazards 2015;79:1–27. https://doi.org/10.1007/s11069-015-1822-7.
[13] Sánchez-Sesma FJ, Pérez-Ruiz JA, Luzón F, Campillo M, Rodríguez-Castellanos A. Diffuse fields in dynamic elasticity. Wave Motion 2008;45:641–54. https://doi.org/10.1016/j.wavemoti.2007.07.005.
[14] Sánchez-Sesma FJ, Rodríguez M, Iturrarán-Viveros U, Luzón F, Campillo M, Margerin L, et al. A theory for microtremor H/V spectral ratio: application for a layered medium. Geophys J Int 2011;186:221–5. https://doi.org/10.1111/j.1365-246X.2011.05064.x.
[15] Sant DA, Karanth RV. Drainage evolution of the lower Narmada valley, western India. Geomorphology 1993;8:221–44. https://doi.org/10.1016/0169-555X(93)90039-5.
[16] Sant DA, Karanth RV. Emplacement of dyke swarms in the lower Narmada Valley, western India. In: Parker AJ, Rickwood PC, Tucker DH, editors. Proceedings of the second international dyke conference A, adelaide, south Australia: publication number 23, international geological correlation program project 257. Rotterdam, Brookfield: A.A. Balkema; 1990; 1990. p. 383–9.
[17] Bedi N, Vaidyanadhan R. Effect of neotectonics on the morphology of the Narmada river in Gujarat, Western India. Z Geomorphol 1982;26:87–102. https://doi.org/10.1127/zfg/26/1982/87.
[18] Sukumaran P, Sant DA, Krishnan K, Rangarajan G. High resolution facies record on late holocene flood plain sediments from lower reaches of Narmada Valley, western India. J Geol Soc India 2012;79:41–52. https://doi.org/10.1007/s12594-012-0009-z.
[19] Sukumaran P, Rajshekhar C, Sant DA, Krishnan K. Late holocene storm records from lower reaches of Narmada valley, Western India. J Geol Soc India 2012;80:403–8. https://doi.org/10.1007/s12594-012-0158-0.
[20] Sukumaran P, Sant DA, Krishnan K, Rangarajan G, Basavaiah N, Schwenninger J-L. Multi-proxy records of late holocene flood events from the lower reaches of the Narmada River, western India. Front Earth Sci 2021;9. https://doi.org/10.3389/feart.2021.634354.
[21] Bard PY, SESAME-Team. Guidelines for the implementation of the H/V spectral ratio technique on ambient vibrations measurements, processing and interpretation. 2004.
[22] Wathelet M, Chatelain JL, Cornou C, Giulio G Di, Guillier B, Ohrnberger M, et al. Geopsy: a user-friendly open-source tool set for ambient vibration processing. Seismol Res Lett 2020;91:1878–89. https://doi.org/10.1785/0220190360.

[23] García-Jerez A, Piña-Flores J, Sánchez-Sesma FJ, Luzón F, Perton M. A computer code for forward calculation and inversion of the H/V spectral ratio under the diffuse field assumption. Comput Geosci 2016;97:67–78. https://doi.org/10.1016/j.cageo.2016.06.016.
[24] Piña-Flores J, Perton M, García-Jerez A, Carmona E, Luzón F, Molina-Villegas JC, et al. The inversion of spectral ratio H/V in a layered system using the diffuse field assumption (DFA). Geophys J Int 2017;208:577–88. https://doi.org/10.1093/gji/ggw416.
[25] Konno K, Ohmachi T. Ground-motion characteristics estimated from spectral ratio between horizontal and vertical components of microtremor. Bull Seismol Soc Am 1998;88:228–41. https://doi.org/10.1785/BSSA0880010228.
[26] Lunedei E, Malischewsky P. A review and some new issues on the theory of the H/V technique for ambient vibrations. Geotechnical, Geological and Earthquake Engineering 2015;39:371–94. https://doi.org/10.1007/978-3-319-16964-4_15.
[27] Matsushima S, Hirokawa T, De Martin F, Kawase H, Sánchez-Sesma FJ. The effect of lateral heterogeneity on horizontal-to-vertical spectral ratio of microtremors inferred from observation and synthetics. Bull Seismol Soc Am 2014;104:381–93. https://doi.org/10.1785/0120120321.
[28] Uebayashi H, Kawabe H, Kamae K. Reproduction of microseism H/V spectral features using a three-dimensional complex topographical model of the sediment-bedrock interface in the Osaka sedimentary basin. Geophys J Int 2012;189:1060–74. https://doi.org/10.1111/j.1365-246X.2012.05408.x.
[29] Claprood M, Asten MW, Kristek J. Combining HVSR microtremor observations with the SPAC method for site resonance study of the Tamar Valley in Launceston (Tasmania, Australia). Geophys J Int 2012;191:765–80. https://doi.org/10.1111/j.1365-246X.2012.05654.x.
[30] Theodoulidis N, Cultrera G, Cornou C, Bard P-Y, Boxberger T, DiGiulio G, et al. Basin effects on ground motion: the case of a high-resolution experiment in Cephalonia (Greece). Bull Earthq Eng 2018;16:529–60. https://doi.org/10.1007/s10518-017-0225-4.
[31] Bell FG. Engineering properties of soils and rocks. Butterworths; 1983.
[32] Arora K. Soil mechanics and foundation engineering. Sixth. STANDARD PUBLISHERS DISTRIBUTORS; 2004.
[33] Anbazhagan P, Uday A, Moustafa SSR, Al-Arifi NSN. Correlation of densities with shear wave velocities and SPT N values. J Geophys Eng 2016;13:320–41. https://doi.org/10.1088/1742-2132/13/3/320.
[34] Wang J, Li X, Rong M, Zhao Q, Kong X. Influence of soil parameter uncertainties on site ambient noise horizontal to vertical spectral ratio modeling. Soil Dynam Earthq Eng 2024;187:108950. https://doi.org/10.1016/j.soildyn.2024.108950.
[35] Piña-Flores J, García-Jerez A, Sánchez-Sesma FJ, Luzón F, Márquez-Domínguez S. HV-Inv: a MATLAB-based graphical tool for the direct and inverse problems of the horizontal-to-vertical spectral ratio under the diffuse field theory. Software Impacts 2024;22:100706. https://doi.org/10.1016/j.simpa.2024.100706.
[36] Maghami S, Sohrabi-Bidar A, Bignardi S, Zarean A, Kamalian M. Extracting the shear wave velocity structure of deep alluviums of "Qom" Basin (Iran) employing HVSR inversion of microtremor recordings. J Appl Geophy 2021;185:104246. https://doi.org/10.1016/j.jappgeo.2020.104246.